International Journal of Multiphase Flow 36 (2010) 691–706

Contents lists available at ScienceDirect

International Journal of Multiphase Flow

journal homepage: www.elsevier.com/locate/ijmulflow

PTV experiments of subcooled boiling flow through a vertical rectangular channel

C.E. Estrada-Perez [a], Y.A. Hassan [a,b,*]

[a] Texas A&M University, Department of Mechanical Engineering, Zachry 129, MS 3133, College Station, TX 77843, USA
[b] Texas A&M University, Department of Nuclear Engineering, Zachry 129, MS 3133, College Station, TX 77843, USA

ARTICLE INFO

Article history:
Received 28 November 2009
Received in revised form 28 April 2010
Accepted 20 May 2010
Available online 26 May 2010

Keywords:
PTV
Convective boiling
Liquid turbulence
Multiphase flow

ABSTRACT

Time resolved Particle Tracking Velocimetry (PTV) experiments were carried out to investigate turbulent, subcooled boiling flow of refrigerant HFE-301 through a vertical rectangular channel with one heated wall. Measurements were performed with liquid Reynolds numbers (based on the hydraulic diameter) of Re = 3309, 9929 and 16,549 over a wall heat flux range of 0.0–64.0 kW/m^2. Turbulence statistics are inferred from PTV full-field velocity measurements. Quantities such as: instantaneous 2D velocity fields, time-averaged axial and normal velocities, axial and normal turbulence intensities, and Reynolds stresses are obtained. The present results agree well with previous studies and provides new information due to the full-field nature of the technique. This work is an attempt to provide turbulent subcooled boiling flow data for validation and improvement of two-phase flow computational models.

1. Introduction

Turbulent subcooled boiling flow has been used extensively in the industry because it is one of the most efficient heat transfer modes. The continuous mixing and stirring of liquid produced during the life cycle of the subcooled boiling bubbles (nucleation, growth, detachment, coalescence and collapsing) are local enhancing mechanisms of heat and momentum transfer. Therefore, liquid turbulence modification produced by these mechanisms, have to be accurately measured and modeled in the numerical correlations/equations used to design energy transfer systems. Multiple experimental efforts have been directed towards this goal, and the literature contains many examples of such works, but for brevity, we will refer to only a few.

Isothermal air–water flow experiments were performed by Lance and Bataille (1991) to understand the influence of the local void fraction, α, on the liquid phase turbulence. They used Laser Doppler Anemometry (LDA) and Hot Film Anemometry (HFA) measurements to study the turbulence of the liquid in a grid-generated, turbulent bubbly flow. They found that the turbulent kinetic energy greatly increases with the void fraction. They described two regimes: the first one corresponds to low values of α, where hydrodynamic interactions between bubbles are negligible, and the second regime to higher α values, in which the bubbles transfer a greater amount of kinetic energy to the liquid. The Reynolds stress tensor shows that the quasi-isotropy was not altered. Furthermore, their one-dimensional spectra analysis showed a large range of high frequencies associated with the wakes of the bubbles and the classical $-1/5$ power law is progressively replaced by a $-8/3$ dependence.

Non-isothermal air–water flow experiments were conducted by Serizawa et al. (1975a,b,c) to study the turbulence structure of upward air–water bubbly flow in a pipe. They used hot film anemometry to measure liquid velocities and liquid turbulence intensities, a double resistivity probe to measure void fraction, bubble impaction rate, and bubble velocities. New principles were presented for measuring the turbulent dispersion coefficient of bubbles and the eddy diffusivity of heat by means of tracer techniques. They found flat radial velocity profiles for both liquid and bubbles; however, the radial void fraction profiles showed a maximum in the near-wall region. For a constant liquid flow rate, the liquid turbulent intensity decreased with increments of gas flow rate. This behavior was seen up to a certain value of the gas flow rate, after which the turbulent liquid intensity started to increase. Furthermore, from their analysis of transport properties, they found that the turbulent transport process is dominated mainly by the liquid phase turbulent velocity component, and that there is systematic increase of heat diffusivity with quality and water velocity.

Non-isothermal single-phase flow experiments were performed to elucidate the effect of density changes on the fluid turbulence within circular and square channels. Barrow (1962) performed single-phase flow experiments in a rectangular channel with unequal heat fluxes in the channel walls. He analyzed the influence of uneven heating on friction and heat transfer coefficients. He measured liquid velocity fields, only for the unheated case. Roy et al. (1986)

* Corresponding author at: Department of Nuclear Engineering, Texas A&M University, Zachry 129, MS 3133, College Station, Texas 77843-3133, USA.
E-mail address: hassan@ne.tamu.edu (Y.A. Hassan).

0301-9322/$ - see front matter © 2010 Elsevier Ltd. All rights reserved.
doi:10.1016/j.ijmultiphaseflow.2010.05.005

performed extensive investigations on heated and unheated R-113 refrigerant through annular channels. Using HFA they obtained mean axial velocity profiles and turbulence intensities for various Reynolds numbers and heat fluxes. They concluded that accurate velocity field measurements in turbulent liquid flow by constant temperature anemometry are difficult since generally only low sensor overheats can be used. Hasan et al. (1992) obtained velocity and temperature fields of heated and unheated refrigerant R-113. Using HFA and a chromel–constantan micro-thermocouple. They presented radial profiles of velocity, turbulence intensities and Reynolds stresses, together with single-point correlations between turbulent velocity and temperature fluctuations. Wardana et al. (1992) used Laser Doppler Velocimetry (LDV) and a resistance thermometer to study air velocity and temperature statistics in a strongly heated turbulent two-dimensional channel flow, with wall temperatures up to 700 °C and a fixed Reynolds number of 14,000. They found that for this conditions ($Gr/Re^2 = 5.25 \times 10^{-5}$, where Gr and Re are Grashof and Reynolds numbers) the normalized mean velocity and mean temperature profiles were not significantly affected by the wall heating. However, they found a suppression of the axial turbulence intensity profile only for points laying on the range ($y/H = 0.2–0.6$). Velidandla et al. (1996) used a two-component LDV and a micro-thermocouple to measure velocities and temperatures of refrigerant R-113. They found buoyancy effects on the time-mean velocity and turbulence fields, even at very low values of Gr/Re^2. Zarate et al. (1998) developed velocity and temperature wall laws in a vertical concentric annular channel from measurements in turbulent liquid flow of refrigerant R-113, noting that when buoyancy forces influence becomes large, the velocity and temperature data do not follow the respective wall laws. Kang et al. (2001) summarized experimental measurements from isothermal and heated turbulent up-flow of refrigerant R-113. They presented liquid turbulence statistics, radial turbulent heat flux distributions and Prandtl number estimations.

One of the early attempts to measure local fields of subcooled boiling parameters of the liquid phase was performed by Roy et al. (1993). They measured turbulent velocity and temperature fields in the all-liquid region adjacent to a subcooled flow boiling layer. Significant changes in the turbulent structure of the all-liquid region were observed due to boiling. Improving their measurement techniques, Roy et al. (1997) were able to measure liquid turbulence statistics of the liquid refrigerant R-113 even within the boiling layer region adjacent to the heated wall. They found that the near-wall liquid velocity field was significantly different from that in single-phase liquid flow at a similar Reynolds number. Lee et al. (2002) performed measurements of subcooled boiling flow of water in a vertical concentric annulus. Using a two-conductivity probe they measured the local void fraction and vapor velocity and with a Pitot tube they measured the liquid velocity. Situ et al. (2004) measured the flow structure of subcooled boiling flow in an annulus. They used a double-sensor conductivity probe method to measure local void fraction, interfacial area concentration and interfacial velocities. Using LDA Ramstorfer et al. (2008) performed subcooled boiling flow experiments in a horizontal channel with one heated wall, to gain insight into the bubble laden near-wall velocity field. Contrary to the vertical channel experiments, they found that the streamwise velocity component was considerably reduced compared to the single-phase case, while the near-wall turbulence was increased due to the presence of the bubbles.

Using the experimental information from the previous studies, different two-phase flow models were developed and used to calculate convective subcooled boiling flow (Roy et al., 2002; Yeoh et al., 2002; Končar et al., 2004; Ramstorfer et al., 2008) with some success. These models share the characteristics of being based on time-average analysis of information from point measurements probes. However, due to the complex nature of the turbulence found in subcooled boiling, this approach seems to be limited. A full-field measurement approach is needed to provide spatial and temporal information.

Visualization techniques such as Particle Image Velocimetry (PIV) and Particle Tacking Velocimetry (PTV) can be used to overcome some of the limitations associated with point measurements techniques. PIV and PTV are non-intrusive and provide full-field quantitative and qualitative information of the flow with high spatial and temporal resolution. The common measuring principle behind these methods is that instantaneous fluid velocities can be evaluated by recording the position of images produced by small tracers suspended in the fluid, at successive time instants. The underlying assumption is that these tracers closely follow the fluid motion with minimal lag. This assumption holds true for a wide variety of flows of interest provided that the tracers are small enough and/or their density approaches that of the fluid. The difference between PIV and PTV is that in PIV, the concentration of tracers is rather high and the measurement of the "local" fluid velocity results from an average over many tracers contained in a measurement volume. This is in contrast with PTV, where the velocity is determined at random locations using the images produced by a single tracer. Although both techniques can be applied on the analysis of two-phase flows, PTV is preferred, due to its ability to differentiate between the gas and liquid phases and subsequently deliver simultaneous velocity fields associated with each phase.

Using visualization techniques in conjunction with PTV, several adiabatic two-phase flow experimental studies were performed (Hassan et al., 2005; Dominguez-Ontiveros et al., 2006; Ortiz-Villafuerte and Hassan, 2006, among others) to investigate the influence of void fraction on liquid turbulence parameters. More recently PTV with high spatial and temporal resolution has been used by Koyasu et al. (2009) to study the liquid turbulence modification by dispersed bubbles in an upward pipe flow. They observed similar trends as those obtained with hot film anemometry (Serizawa et al., 1975b). They concluded that dissipative eddies around small bubbles increased the dissipation rate of turbulence kinetic energy and eddies from large bubbles augmented the turbulence kinetic energy.

These studies elucidate the phenomenological events important for the modeling of two-phase flows. However, there appears to be a scarcity of subcooled boiling experimental studies that can capture instantaneous whole-field measurements with a fast time response. In this study, time-resolved PTV experiments are performed to obtain liquid flow measurements in turbulent subcooled boiling flow of refrigerant HFE-301 3M (2009) through a rectangular channel. This investigation is an attempt to obtain a database on turbulent subcooled boiling flow for validation and improvement of two-phase flow computational models.

2. Experimental rig

The experimental facility was designed for the visualization of subcooled boiling flow of refrigerant HFE-301 at low system pressure. Fluid selection justification and experimental setup details are given in the following sections.

2.1. Fluid selection and scaling

The selection of the working fluid was based on a scaling analysis of thermodynamic properties. Scaling can be achieved by using critical fluid properties such as critical density, temperature or pressure. It has been shown (Mayinger, 1981) that the critical pressure ratio p/p_c is the most useful parameter for many applications,

including scaling between water and refrigerants. Scaling with the critical pressure ratio provided good similarity only for some fluid properties while for others a correction was needed. As an example, Fig. 1 shows the comparison of scaled thermodynamic properties of water and HFE-301 at saturation conditions. Fig. 1a shows the two-phase flow density ratio (ρ_L/ρ_v) scaled with the critical pressure ratio. There is only a deviation of a few percent in the two-phase flow density ratio for water and HFE-301; however, when comparing the liquid viscosities μ_L in Fig. 1b, a larger discrepancy is found. A multiplication factor (k_4) is used to correct for this discrepancy. Fig. 1b shows that liquid viscosities for both fluids are comparable after applying the correction factor (black dotted line). This correction factor then must be considered in the estimation of dimensionless numbers. Also shown in Fig. 1 are three conditions on which HFE-301 may be used to simulate water. Condition 1 was selected to perform the HFE-301 boiling experiments, simulating the behavior of a geometrically similar water system at a pressure of about 9 bars and saturation temperatures of 175 °C. Conditions 2 and 3 are of importance for the nuclear industry, they represent typical operational conditions of Boiling and Pressurized Water Reactors (BWR, PWR), respectively. Table 1 shows saturation pressure and temperature values for both water and HFE-301 for each condition.

Table 1
Important operation conditions and corresponding values for HFE-301 refrigerant and water.

Condition No.	P_{HFE} (bar)	$Tsat_{HFE}$ (°C)	P_{H_2O} (bar)	$Tsat_{H_2O}$ (°C)
1	1.00	36.00	8.95	175.13
2	7.80	107.00	70.00	285.83
3	16.08	141.00	140.00	336.67

2.2. Hydraulic loop

The hydraulic loop consists of an external loop and a test section, both designed to withstand temperatures in excess of 200 °C, and pressures up to 100 psi. The external loop provides thermal and hydraulic steady state conditions. The temperature of the fluid inlet is controlled with a Watlow circulation heater, managed by an internal PID temperature controller, capable of a fast response to temperature changes. The system excess energy is removed with a small plate heat exchanger connected to a chilling system. The mass flow rate to the test section was measured with a variable area flow-meter and controlled by adjusting the test section valves. The test section is a rectangular channel made of transparent polycarbonate 530 mm long with a cross-sectional area of 8.7 × 7.6 mm^2. The test section dimensions were selected to approximate those typically found in coolant channels of boiling and pressurized water nuclear reactors (BWR, PWR) Energy for boiling was provided by a Kapton thin heater with a length and width of 175 mm and 7 mm, respectively, and a maximum working temperature of 200 °C. The heater is attached to the lateral interior face of the channel (see Fig. 2). The electric current to

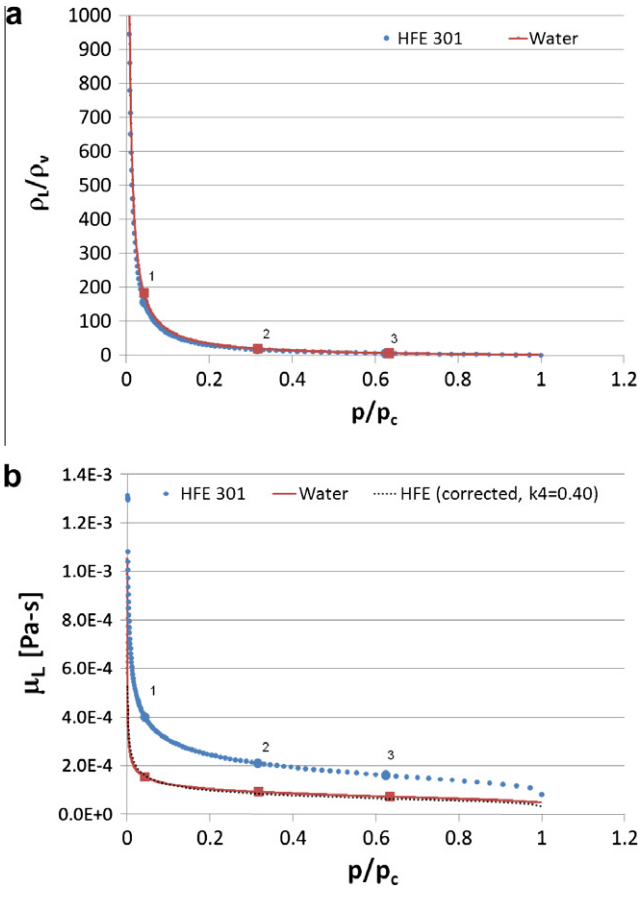

Fig. 1. Comparison of thermodynamic properties of water and HFE-301 as a function of reduced pressure.

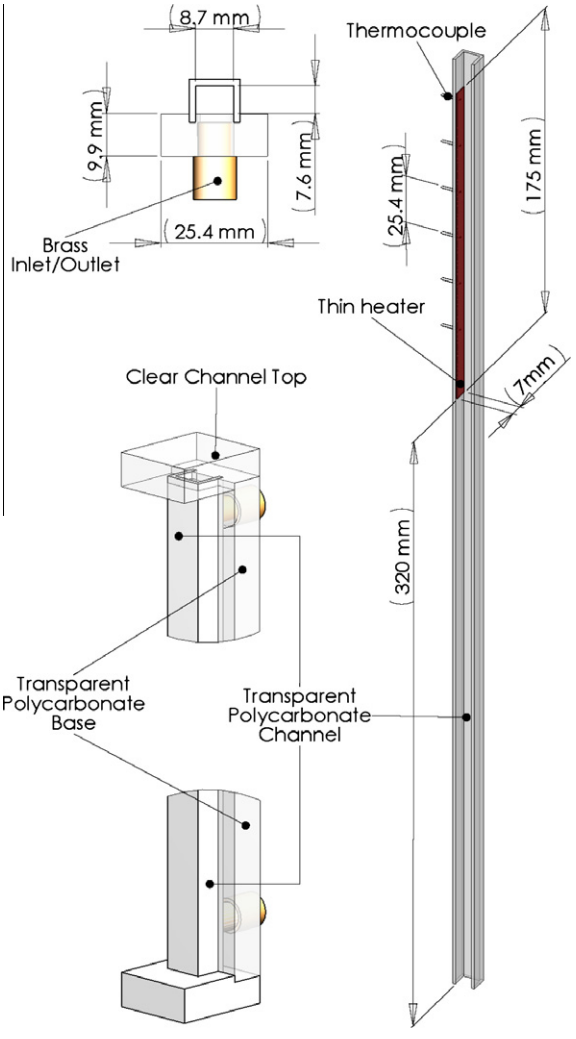

Fig. 2. Test section schematics and dimensions.

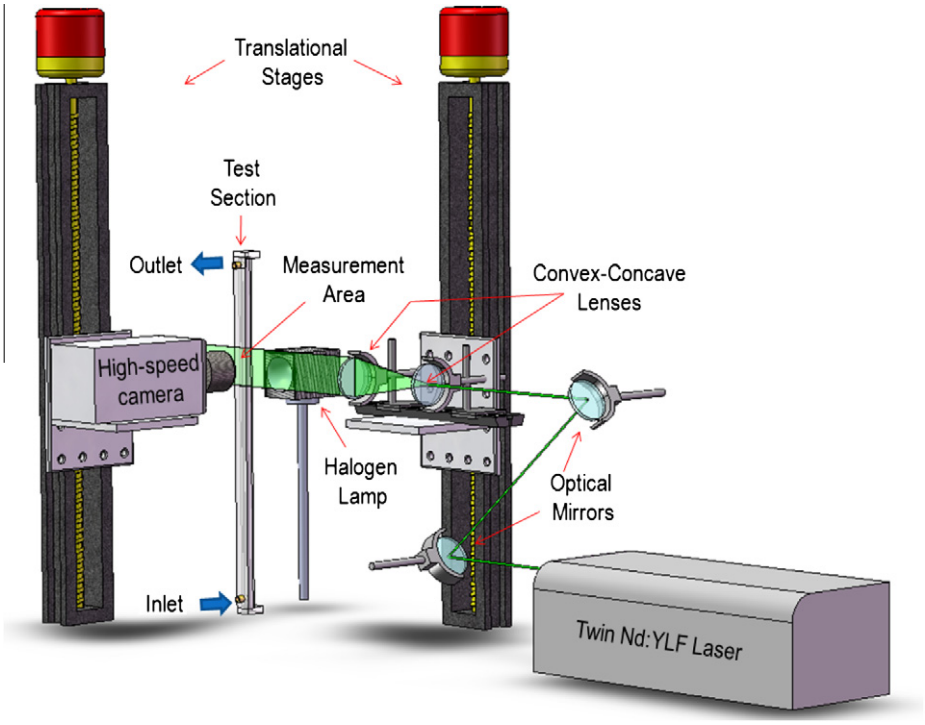

Fig. 3. Visualization system schematics.

the heater is provided and adjusted by a DC power supply, from which a maximum wall heat flux of 64 kW/m^2 was measured. To reduce heat losses to the ambient, the external face of the channel was insulated with 10 mm of balsa wood. With this configuration an unheated length of 320 mm is achieved. To measure the heater wall temperature, six J-type thermocouples were attached to the external face of the heater in a vertical arrangement along the heater wall with a space of 25.4 mm in between them. Test section fluid inlet (T_{in}) and outlet (T_{out}) temperatures were also measured by two J-type thermocouples. Fig. 2 shows the schematics and dimensions of the test section.

2.3. Visualization system

The visualization system consisted of a high-speed high-resolution camera, a high-speed high-power laser, a continuous halogen lamp,[1] mirrors, translational stages, lenses and particle flow tracers. The high-speed camera has a maximum frame rate of 4700 fps at a resolution of 800 × 600 pixels, with a maximum bit depth of 12 bits. The illumination was provided by a Pegasus dual lamp laser which can operate at a maximum power of 27 mJ/pulse. A maximum pulse rate of 20,000 pulse/s can be also achieved. Two optical mirrors and two concave–convex lenses are used to convert the small circular beam from the laser, into a 1 mm thick sheet of light. The laser light sheet is positioned on the measurement region, parallel to the camera focal area. The camera, mirrors and lenses are mounted on translational stages to have the capability of changing the measuring region along the test section. The flow tracers are highly reflective silver coated particles with a density range of 1.39–1.41 g/cm^3, with an average particle diameter of 40 μm. Fig. 3 shows the schematics of the visualization system.

[1] The halogen lamp provided illumination for shadowgraphy measurements from which bubble dynamics can be determined. However, for the sake of brevity, shadowgraphy results are not shown.

3. Velocity measurement system and accuracy

3.1. PTV algorithm

In this study, the PTV algorithm used to analyze subcooled boiling flow is a home-developed routine that has been applied successfully in several previous two-phase flow investigations (Hassan et al., 2005; Dominguez-Ontiveros et al., 2006; Ortiz-Villafuerte and Hassan, 2006). The original algorithm was developed by Canaan and Hassan (1991), and has been improved over the years. A simplified version of the PTV algorithm performs: (1) particle detection, (2) particle centroid location estimation and (3) particle matching in between consecutive frames (particle tracking). In this section, the components of the PTV algorithm that are new or relevant for the present study are described. A more detailed description of the PTV algorithm can be obtained from Estrada-Perez (2004).

3.1.1. Particle detection

The particle detection procedure is particularly important in multi-phase flow experiments where accurate identification and discrimination between phases is required. In this study a particle mask correlation method (Takehara, 1998) is implemented. This technique is an image template matching routine, where the selected template is generated from a Gaussian representation of an ideal particle given by the following equation:

$$I(x,y) = I_0 \exp\left[-\frac{1}{2r_0^2}\left(\frac{(x-x_0)^2}{a^2} + \frac{(x-x_0)(y-y_0)}{c^2} + \frac{(y-y_0)^2}{b^2}\right)\right] \quad (1)$$

where $I(x,y)$ is the gray scale intensity at the (x,y) position, (x_o,y_o) is the particle centroid location, I_o is the maximum intensity, a, b, and c are shape modifier parameters, and r_o is the particle radius. The image template selection depends on the object of interest, for example, selecting a small value for r_o (particle size) will in turn

provide an approach of discrimination between small and large objects.

3.1.2. Particle centroid estimation

Once a particle is identified, its centroid is estimated to sub-pixel accuracy. In this study three different centroid estimation techniques are available: three point Gaussian interpolation (3PGI) (Willert and Gharib, 1991), two-dimensional Gaussian regression (2DGR) (Noback and Honkanen, 2005), and center of mass technique (CMT). 3PGI and 2DGR performance and accuracy are similar as both are well suited for small (radius <10 pixels) Gaussian shaped objects. The CMT is better suited for larger objects (radius >10 pixels) without shape restriction. In a two-phase flow PTV experiment, CMT will be ideal for the location of bubbles centroid, while 3PGI and 2DGR are well suited to estimate the liquid tracer particles centroids. Although 3PGI technique is the most commonly used among researchers due to its simplicity, in this work, 2DGR is preferred since it relies on more information (9 pixels are used in the regression rather than 6) to estimate the centroids.

3.1.3. Particle tracking

The particle tracking algorithm is based on direct spatial correlation. This algorithm computes a correlation coefficient between two sub-images of single-exposed PTV pictures. The correlation coefficient between the two sub-images I_A and I_B with $a \times b$ dimensions is computed using the following relation:

$$C_{I_A I_B}(x_o, y_o) = \sum_{i=1}^{a}\sum_{j=1}^{b}[I_A(i,j) - \bar{I}_A][I_B(i,j) - \bar{I}_B] \times \left(\sum_{i=1}^{a}\sum_{j=1}^{b}[I_A(i,j) - \bar{I}_A]\right)^{-1/2} \times \left(\sum_{i=1}^{a}\sum_{j=1}^{b}[I_B(i,j) - \bar{I}_B]\right)^{-1/2} \quad (2)$$

where $\bar{I}_A$ and $\bar{I}_B$ are the average intensities of sub-images A and B, respectively. Assuming two experimental pictures A and B, acquired at two different times $t = t_o$ and $t = t_o + \Delta t$, respectively, the correlation coefficient will determine which particle in picture B is the best match of a particle on picture A. Since particles location is estimated to sub-pixel accuracy, and the interval between pictures is known, an accurate particle velocity estimation is achieved.

3.2. PTV algorithm accuracy

The accuracy of the PTV algorithm used in this work has been extensively tested and benchmarked against synthetic and experimental data. A version of this program was used in the PIV Challenge 2005 (Stanislas et al., 2008), where it was shown that for suitable PTV images (low particle density images as in Case A1 of the PIV Challenge 2005), the algorithm bias and RMS errors (as defined in Section 3.2.2) for both velocity components accounts for 0.0001 and 0.1056 pixel/Δt, respectively (with Δt = time between frames). To further test the accuracy of the PTV algorithm, and to discern experimental conditions which exhibited a lesser error, a sensitivity analysis was performed by Estrada-Perez (2004). The sensitivity analysis was performed with home-made artificial images. These images were created simulating ideal conditions to test specific algorithm performances. Particle positions, sizes and displacements were varied. Since particles positions and velocities were known, the experimental parameters that have high impact on the measurements accuracy were identified. Some of the relevant results are summarized below.

3.2.1. Particle detection and centroid estimation errors

Fig. 4a shows the centroid estimation error as a function of particle size. For the boiling experiments, the average particle image radius was about 2 pixels, where the minimum algorithm error (RMS $\approx$ 0.002 pixel) is located. This optimal size was obtained with a trade-off between camera magnification, resolution and particle dimensions. Since particle dimensions and camera resolution are fixed (30–40 μm and 800 × 600), the required magnification provided a visualization area of 9.87 × 7.40 mm^2 with 81.03 pixel/mm. Fig. 4b presents centroid estimation error as a function of particle image density using a fixed particle radius of 2 pixels. As expected, increasing particle image density increases the centroid estimation error. Having crowded pictures with particles images close and overlapped, results in difficulty distinguishing individual particles from their neighbors. In the boiling experiments, an average of 3000 particles in a 800 × 600 image (equivalent to 1562 particles in a 500 × 500 image) was obtained. This corresponds to a RMS error for the centroid location of about 0.02 pixels (≈0.3 μm). Fig. 4c shows the effectiveness of the particle detection algorithm. Both 2DGR and 3PGI estimation techniques have acceptable performances even for high particle image densities. These techniques accurately detect and estimate the centroid of overlapped particle images. CGT technique lacks this capability, therefore, overlapped particles will be considered as a single particle; consequently both efficiency and accuracy are degraded. For the boiling experiments, 2DGR technique was used. The experimental particle image density was 1562 particles per image. This provided an experimental particle image detection efficiency of about 98%.

3.2.2. Accuracy of velocity estimation

To analyze the PTV algorithm velocity measurement error, a procedure similar to the one presented by Astarita and Cardone (2005) was employed. Home-made synthetic images were used to estimate the influence of particle concentration and displacement on the velocity measurements accuracy. Gui and Wereley (2002) identified three types of errors: bias (β), random (σ) and total error (δ). By using synthetic images, the exact displacement field is known, thus these errors can be quantified as follows:

$$\beta = u - \bar{u} \quad (3)$$

$$\sigma = \sqrt{\frac{1}{N}\sum_{i=1}^{N}(u_i - \bar{u})^2} \quad (4)$$

$$\delta = \sqrt{\frac{1}{N}\sum_{i=1}^{N}(u_i - u)^2} \quad (5)$$

where $\bar{u}$ is the mean measured displacement value, u is the exact imposed displacement, u_i the measured displacement, and N is the number of samples. Knowing that the bias and random errors are contained within the total error ($\delta^2 = \beta^2 + \sigma^2$), only the total error is considered. Sets of 100 images with 512 × 512 resolution were generated, with a particle radius of 2 pixels (to obtain the minimum error in the particle centroid location). Four cases were considered, each with a particle image density of 2500, 5200, 8200 and 10,000 particles per image. An interrogation window of 32 × 32 pixels was selected for correlation computation. Therefore, for each case, the average number of particles within the interrogation window (NI) was NI = 9.76, 20.31, 32.03, and 39.06. Correlation based algorithms are affected by a bias error with a periodic pattern of one pixel wavelength causing a measurement bias toward integer values (peak locking). It is known that the source of this kind of error must be ascribed to the particle image pixelization and in the consequent discrete nature of the correlation signal (Scarano and Riethmuller, 2000). This periodic behavior, typical of iterative methods, is observed also for the present algorithm. In Fig. 5 the total error as a function of the imposed particle displacement for the different image densities is shown. The periodic behavior of the total

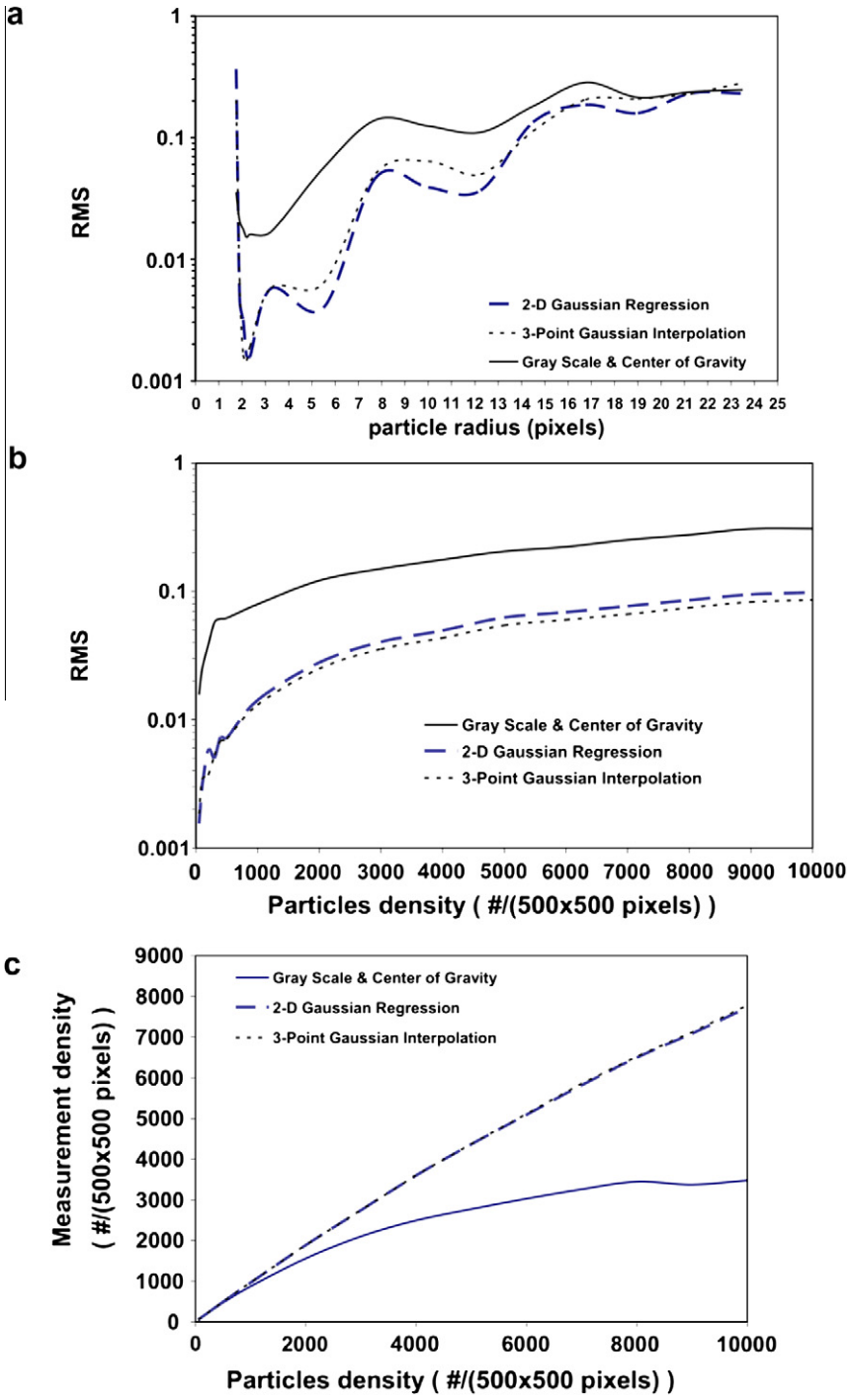

Fig. 4. Centroid estimation error sensitivity analysis.

error is similar for the different imposed displacements, but with larger amplitude for the higher particle image density cases. Fixed maximum and minimum errors are found no matter the imposed displacement. Particle image density plays an important role in the PTV accuracy, as seen in Fig. 5, the lowest particle image density case leads to lower values for δ because no particle overlapping occurs and image pattern lost is reduced. It is clear that the maximum total error on the velocity is below 0.02 pixel/Δt (even for the high particle density cases). This error is about the same as the one encountered for the centroid location error. However it has to be considered that on the calculation of the velocity error, about 20% of the particles had bad centroid detection or bad particle matching between frames, leading to spurious vectors that were eliminated based on a statistical analysis. This analysis provided a confirmation that in the boiling experiments, the particle image sizes, density and displacements were within ranges that induce acceptable error values; therefore, a conservative estimation for the boiling experimental error on the velocity measurement will account for 0.1 pixel/Δt or 0.004 m/s (about 0.26% of the maximum axial velocity).

4. Influence of visualization devices on temperature measurements

The fluid turbulence modification due to changes of wall heat flux can not be correctly assessed without an estimate of the

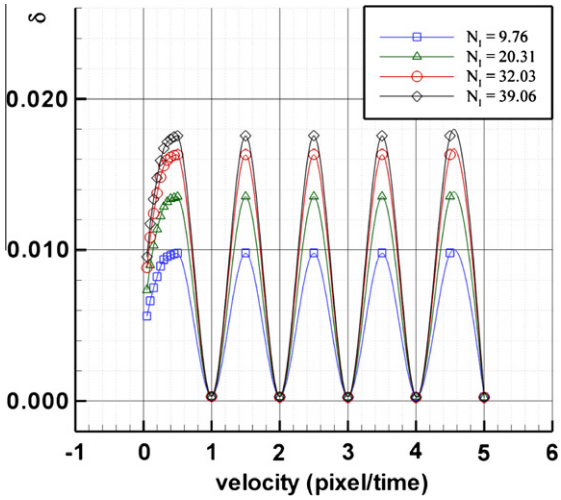

Fig. 5. Measured velocity total error for different particle velocities.

addition or loss of energy provided by the flow visualization devices. To this end, convective boiling experiments with Re = 9929 and heater power values (Q_H) of 0.0, 4.98, 15.13, 45.42, and 80.56 W were performed considering four different cases: (a) reference (with no visualization devices), (b) flow with particle tracers, (c) flow when halogen light illumination is on, and (d) flow when laser light illumination is on. In these experiments three hours were used as a steady state waiting time, after which, temperature measurements were acquired for 10 s at a rate of 1000 Hz. The heater wall temperature at different heights, the channel inlet and outlet fluid temperatures and the ambient air temperature were measured for each case. Fig. 6 shows a comparison of the heater average wall temperatures for the different cases. The maximum relative and absolute differences with respect to the reference case are shown in Table 2. There are not noticeable differences on the measured temperatures within the cases. The laser light induced the largest wall temperature increase with respect to the reference case; the absolute difference accounted for 2.18 °C which is lower than the thermocouples tolerance. Fig. 7 shows the effects of the illumination devices on the difference between inlet and outlet liquid temperatures ($\Delta T_f = T_{out} - T_{in}$) for different heater powers. The effect of the illumination devices on ΔT_f is also negligible, having a maximum absolute difference value of 0.15 °C. Although the effect of the illumination devices on the overall heat transfer of the system is negligible and within the values of the temperature measurement uncertainties, further investigations are needed to determine the local effects induced by the illumination devices.

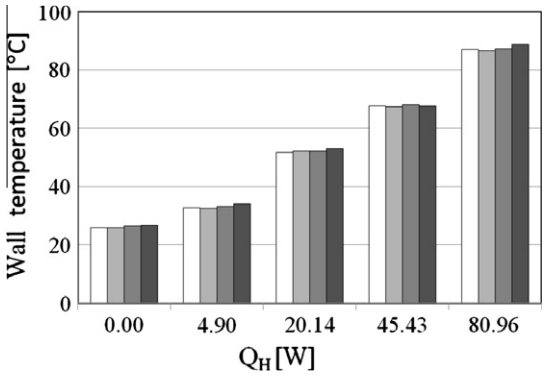

Fig. 6. Wall temperature comparison for case: (a) reference □, (b) PTV particles ■, (c) halogen illumination ■, (d) laser illumination ■.

Table 2
Maximum relative and absolute wall temperature differences with respect to the reference case.

Device	Relative difference (%)	Absolute difference (°C)
PTV particles	2.23	1.56
Halogen lamp	4.11	1.09
PTV laser	6.53	2.18

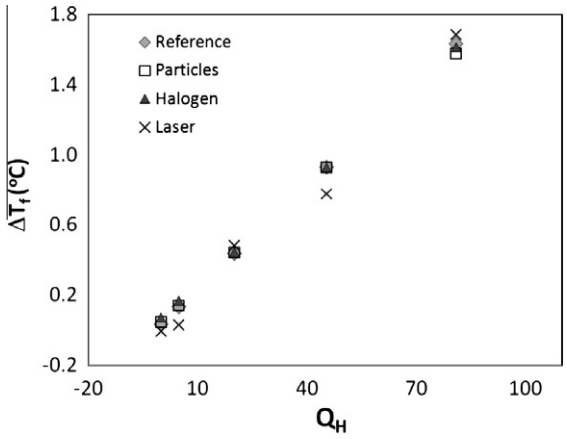

Fig. 7. Differences between channel outlet and inlet fluid temperatures measured for each different illumination case for different heater powers.

5. Experimental uncertainties

A variable area flow-meter model F-450 from Blue-White industries, was used to measure the volumetric flow rate through the test section. The full-scale accuracy accounts for ±5%. Additional corrections were needed since water was used for the flow-meter factory calibration. The correction formula for a working fluid with density of 1400 kg/m^3 is $\dot{Q}_C = \dot{Q}_M \times 0.6842$, where $\dot{Q}_C$ and $\dot{Q}_M$ are the corrected and the measured volumetric flow rates.

Temperature measurements were performed with J-type Omega thermocouples with ±2.25 °C tolerance or 0.75% of the measured temperature within the range −40 °C and 375 °C. In the boiling experiments, the outside heater wall temperature was measured with six thermocouples attached along the heater wall (see Fig. 2). Direct measurements of inside wall temperature were not performed to avoid flow disturbances in the near-wall region. To estimate inside wall temperature from the outside wall temperature measurements, a calibration curve was experimentally obtained. For the calibration experiments, two thermocouples were used; one to measure the outside heater wall temperature (T_{Ho}) and the other to measure the inside heater wall temperature (T_{Hi}). Different flow rates and heat fluxes were considered to cover the full range of experimental conditions. It was found that the wall temperature ratio was always close to $T_{Ho}/T_{Hi} = 1.3$. The heater power was calculated as the product of the current and the voltage difference across the heater. The DC power supply (Mastech D.C. HY3020MR) voltage and current reading accuracy accounted for ±1% and ±2%, respectively, from which a heater power measurement accuracy of ±2.23% was calculated with the error analysis suggested by Kline and McClintock (1953). The heat losses from the test section to the ambient were calculated with a heat balance from experimental data obtained under no-liquid, no-flow conditions, with power ranges from 5.01 to 13.72 W. Fig. 8 shows the percentage of heat loss (Q_{LOSS} %) as a function of temperature difference between wall heater temperature (T_H) and ambient temperature (T_∞). The maximum temperature difference ($T_H - T_\infty$) in

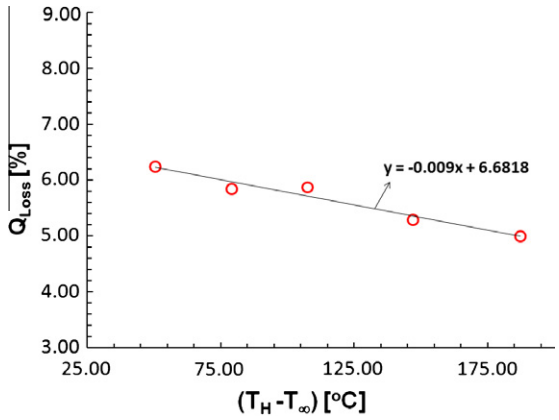

Fig. 8. Percentage of heat loss as a function of temperature difference ($T_H - T_\infty$).

the boiling flow experiments is about 65 °C. At these conditions an average heat loss of about 6% was found.

Additional sources of error for PTV measurements are induced by gravitational forces when flow tracers density differs largely from that of the liquid. An indication of the influence of gravitational forces, can be obtained from Stokes drag law (Riethmuller, 2000), from which the gravitational induced velocity U_g is given by

$$U_g = d_p^2 \frac{(\rho_p - \rho)}{18\mu} g \tag{6}$$

where d_p and ρ_p are diameter and density of the particles, ρ and μ are the density and dynamic viscosity of the liquid, and g is the gravitational acceleration. In the subcooled boiling experiments the liquid density gradient induced a maximum gravitational velocity of $U_g = 2.4$ μm/s, therefore the influence of liquid density changes on velocity estimation can be neglected.

Another factor affecting the PTV accuracy of the non-isothermal experimental cases is the "aero-optical" distortion effect (Elsinga et al., 2005). Optical distortions appear when the illuminated particles are observed through a medium that is optically inhomogeneous due to a large density gradient. The resulting particle image pattern is subjected to deformation and blur. Two forms of error can be identified: position error and velocity error. Considering a 2D optical distortion theory, the expression for the particle position error due to optical distortion ($\vec{\xi}(\vec{y})$) simplifies to

$$\xi_y = -\frac{1}{2} W^2 \frac{dn}{dy} \tag{7}$$

and the velocity error due to optical distortion is given by

$$\Delta v(y) = -\frac{dv}{dy} \xi_y \tag{8}$$

Since dn/dy is not directly known for the refrigerant HFE-301 an expression relating the refractive index and the temperature is used. It is assumed that the change of refractive index as a function of temperature is given by

$$\frac{dn}{dT} = -0.00045 \frac{1}{^\circ C} \tag{9}$$

This equation is a good approximation for most organic compounds, therefore

$$\frac{dn}{dy} = \left(-0.00045 \frac{1}{^\circ C}\right) \frac{dT}{dy} \approx \left(-0.00045 \frac{1}{^\circ C}\right) \frac{\Delta T}{\Delta y} \tag{10}$$

Assuming the maximum value for $\Delta T = T_{sat} - T_c$, where T_{sat} is the liquid saturation temperature equal to 34 °C, and T_c is the average liquid temperature with a value of 29.77 °C (obtained from experimental measurements) then $\Delta T = 4.23$ °C. Considering Δy as the half height of the channel = 4.3 mm, and considering $W = 3.8$ mm (distance from laser plane to the channel wall), the maximum optical displacement error is $\xi_{y_{max}} = 3.5$ μm or 0.28 pixels.

The velocity error can be expressed as:

$$\Delta v(y) = \frac{dv}{dy} \xi_y \approx \frac{\Delta v}{\Delta y} \xi_y \tag{11}$$

Again, Δy = half height of the channel = 4.3 mm and $\Delta v \approx 0.01$ m/s as obtained from experimental values; therefore, a maximum velocity error value is estimated to be $\Delta v_{max} = 8.1$ μ m/s or 0.65 pixels/s. This error represents about 0.07% of the normal velocity, and about 0.004% of the axial velocity.

Further investigation of the PTV velocity measurement accuracy was performed by comparing PTV measurements with the flow meter readings. The average velocity obtained with PTV was 10% larger than that measured by the flow meter. This discrepancy is attributed to the fact that PTV measurements were acquired in the center plane of the channel, where the maximum velocity is located. If more planes were considered for the PTV measurements, then this discrepancy should decrease.

Sampling number is another factor that influences the velocity measurement accuracy. In this study, the sampling number corresponds to the number of PTV velocity fields (or number of PTV image pairs) used to estimate the liquid average velocities. The sampling number influence on the velocity measurement uncertainty is estimated experimentally as shown in Fig. 9, where $\Delta\overline{X}(\overline{X} : \overline{U}, \overline{V})$ is defined as

$$\Delta\overline{X} = \frac{\overline{X} - \overline{X}_m}{\overline{X}_m} \tag{12}$$

In this case, $\overline{X}$ is the average value calculated using N velocity fields and $\overline{X}_m$ is the mean value of $\overline{X}$ for the case with a number sampling of $N = 5000$.

As shown in Fig. 9 the average normal velocity uncertainty is less than 5% after a sampling number $N = 3000$, while the average axial velocity uncertainty is less than 0.5% after a sampling number $N = 250$; therefore, in this study, a sampling number of 5000 is used to yield reasonable statistical estimations of the flow average velocities.

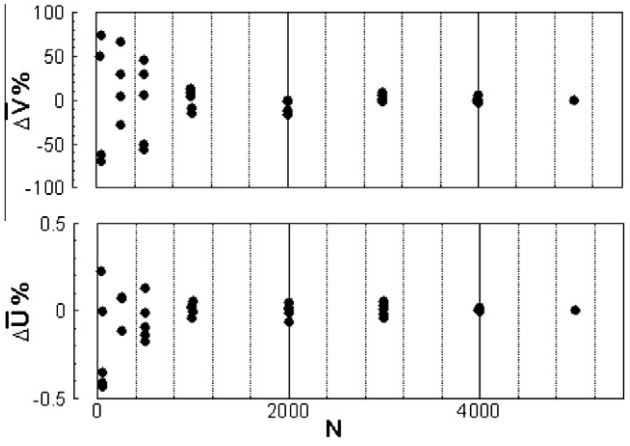

Fig. 9. Sampling number effect on velocity measurements uncertainty.

6. Experimental approach

6.1. Flow characteristics, single-phase

To characterize the flow, single-phase unheated liquid velocity measurements were performed using PTV at three different axial positions along the channel length. The distances from the measurement region positions with respect to the channel inlet are shown in Table 3.

At each measurement region, 5000 images were acquired using the high speed camera. The camera was synchronized with the high energy laser. The camera frame rate was 2500 fps with an exposure time of 2 μs. Each image consisted of 504 × 800 pixels resulting in a spatial resolution of 20.1 μm/pixel. A Reynolds number (Re) of 9929 was considered in this experiment, and a constant inlet temperature of 25.5 °C was maintained at atmospheric pressure. Fig. 10 shows the mean axial velocity $\overline{U}$ and its turbulence intensity u' distribution, both normalized by the mean centerline axial velocity ($\overline{U_c}$). The distance from the wall is normalized by the channel half-height (h). No significant differences were found between the different measurement locations, only small discrepancies of the turbulence intensities in the near-wall region were observed. This analysis presents sufficient evidence of a fully developed flow. Ideally, for two-dimensional fully developed flow, the mean normal velocity $\overline{V}$ should be zero; however, in this experiments nonzero values of this velocity were measured, but were only about 0.7% of the mean axial velocity component. Measurement region P56 at 455 mm from the channel inlet (see Table 3) presented fully developed flow statistical characteristics. Consequently, it was selected as a suitable measurement area for the boiling experimental investigations.

Table 3
Test section measurement regions.

	Distance from the inlet (mm)	L/D_h	Symbol
P56	455	56	×
P23	365	45	■
N10	275	34	▲

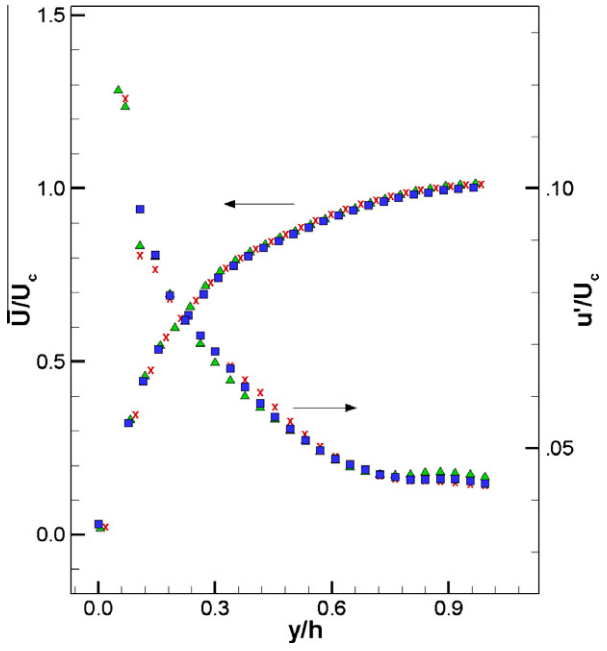

Fig. 10. Axial mean velocity $\overline{U}$ and axial turbulence intensity u' profiles at various axial locations from the inlet: 455 mm ×, 365 mm ■, and 275 mm ▲, from the channel inlet.

6.2. PTV experiments

The measurement area selected was located at 455 mm (position P56) from the channel inlet. PTV measurements to obtain liquid flow velocities were performed at this position, which is equivalent to $L/D_H = 56$. A camera frame rate of 3500 fps, and an exposure time of 2 μs were selected. Each acquired image consisted of 600 × 800 pixels with a spatial resolution of 12.3 μm/pixel. Three different Reynolds numbers were considered: 3309, 9926 and 16,549. For each Reynolds number condition, about 13 different heat fluxes (q'') were imposed ranging from 0.0 to 64.0 kW/m^2. With the help of the shadowgraphy images (see Section 2.3) important bubble dynamics can be determined. For example, the onset of nucleate boiling for the lowest Reynolds number (Re = 3309) was observed at a heat flux $q'' = q''_{ONB} = 3.9$ kW/m^2, and was located at 20 mm from the beginning of heating (at 420 mm from the channel inlet), with an average departure bubble diameter of $D_{dep} = 0.31$ mm, and a bubble departure frequency of 77 Hz. The average bubble diameter at the measurement position (position P56) was $D_B = 1.78$ mm with an average velocity of 0.2 m/s. More detailed information can be acquired from the shadowgraphy images. However, for the sake of brevity, this information is not provided. For all cases a constant inlet temperature of 25.5 °C was maintained. The heater wall average temperature and fluid outlet temperature were also measured.

Fig. 11 shows the experimental images obtained from the PTV experiment at a Re = 9929. Fig. 11a presents the unheated single-phase flow images, where the flow seedings are easily identified from the black background. The heated single-phase experimental images are similar and are not shown for brevity. Fig. 11b presents

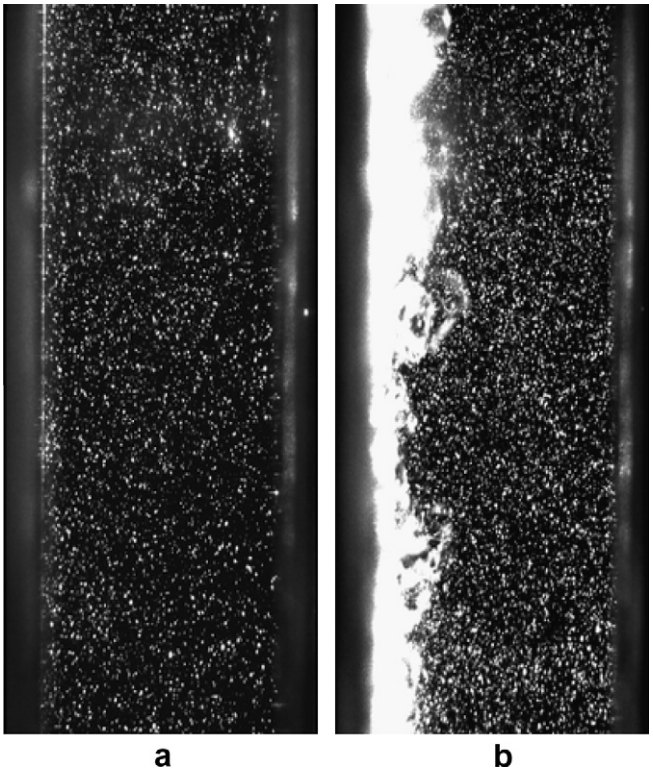

Fig. 11. PTV experimental images: (a) unheated single-phase flow, (b) boiling flow with $q'' = 56.9$ kW/m^2.

an example of the boiling flow images with a heated condition of $q'' = 56.9\ kW/m^2$. A bubble layer is shown on the left side of the channel where boiling occurs. From these images, bubbles can be easily discriminated from the flow seedings due to differences in size, gray scale value and shape.

Fig. 12 shows instantaneous velocity fields obtained from experimental images at Re = 9929. Fig. 12a presents the velocity field from the unheated single-phase flow experiments. Fig. 12b presents the velocity field obtained from the boiling flow experiment with $q'' = 56.9\ kW/m^2$. No velocity vectors were obtained at positions fully occupied by bubbles, confirming that only the liquid velocity is being tracked. It is also noted that the velocity magnitude is larger in regions close to the heated wall (left part of the channel).

7. Results

7.1. Heat flux influence on the liquid-phase behavior

Wall heating brought changes in the velocity distribution profiles. Some of these changes are general trends observed also in other studies (Roy et al., 1993; Wardana et al., 1994; Lee et al., 2002) and are summarized here: First, the mean liquid axial velocity in regions close to the heated wall increases accompanied with a decrease in the axial velocity for regions far from the heated wall. Second, there is a marked shift of the maximum liquid axial velocity location toward the wall. These trends are also observed in Fig. 13. Fig. 13a shows the profiles of mean liquid axial velocity $\overline{U}$ for Re = 3309 with wall heat fluxes ranging from 0 to 64 kW/m^2. It is observed that for wall heat fluxes ranging from 3.9 to 9.0 kW/m^2 the increase of velocity close to the wall shifted the maximum towards a common position located at about $y = 2.5$ mm. These heat fluxes shared a common maximum velocity magnitude of approximately 0.2 m/s. Further increase in the heat

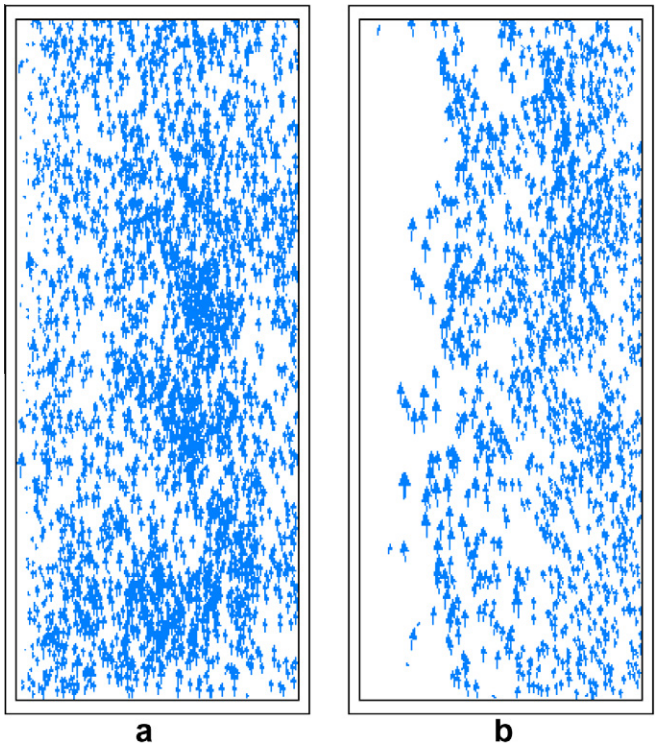

Fig. 12. Velocity fields obtained from experimental images for: (a) unheated single-phase flow, (b) boiling flow with $q'' = 56.9\ kW/m^2$.

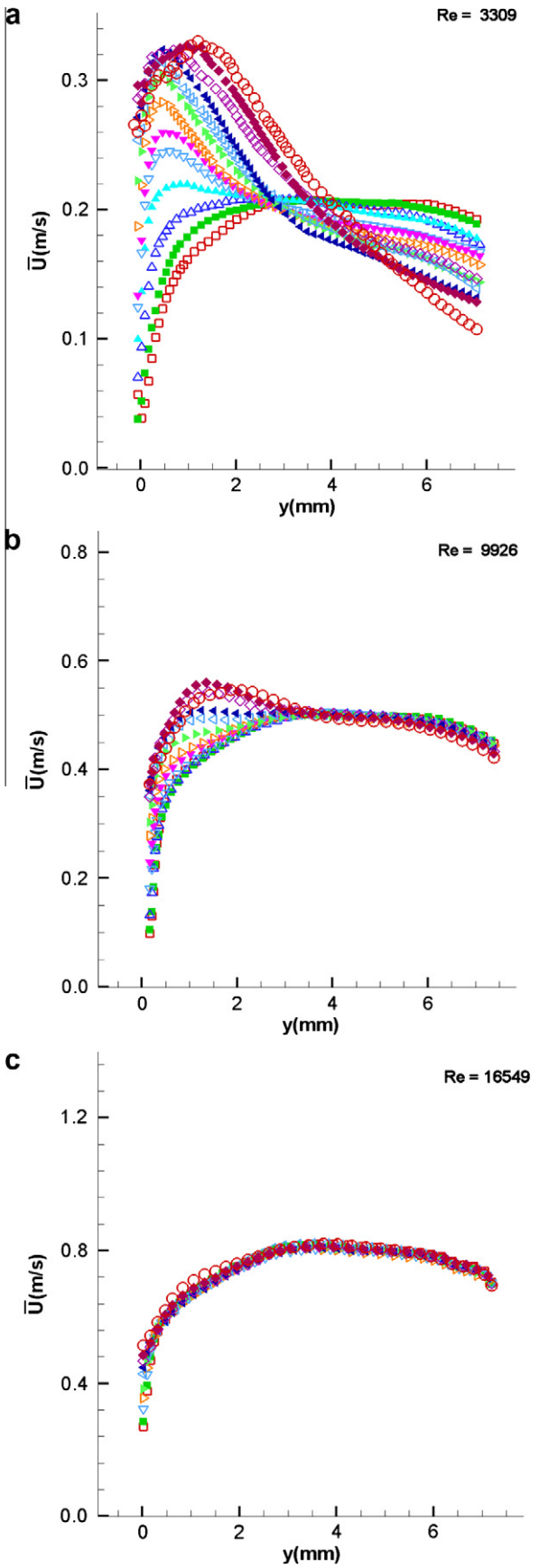

Fig. 13. Mean axial liquid velocity profile for: (a) Re = 3309, (b) Re = 9926, (c) Re = 16,549 with $q'' = 0.0$ □, 3.9 ■, 9.0 △, 12.2 ▲, 16.0 ▽, 18.3 ▼, 20.3 ▷, 22.3 ▶, 35.9 ◁, 42.3 0,0,0.65 ◀, 48.7 0.66,0.0,0.66 ◊, 56.9 ♦, 64.0 ○ (kW/m^2).

flux forced the maximum velocity magnitude to increase and to shift closer to the wall ($y \sim 0.5$ mm). This behavior is observed up to a heat flux of 42.3 kW/m^2. The velocity profiles for these heat fluxes intersected at a common position ($y = 2.5$ mm). The general trends previously mentioned changed for the highest heat flux cases (from 48.7 to 64.0 kW/m^2). For these cases new trends were found: first, the maximum liquid axial velocity reaches a "terminal" maximum velocity of about 0.34 m/s, and second, the maximum liquid axial velocity starts shifting away from the wall towards the center of the channel. Furthermore, the common intersecting point found in the lower heat fluxes ($y = 2.5$ mm) is not present in the higher heat flux cases. Instead, a shifting of this point towards the center of the channel was observed. Similar trends were also observed for the medium Reynolds number case (Re = 9929) shown in Fig. 13b. For this Reynolds number, the influence of wall heat flux over the axial velocity follows the same general trends as observed for the lower Reynolds number case (Re = 3309); however, the increase of axial liquid velocity due to the increase of wall heat flux is lower, and the velocity reduction effect for regions far from the wall is present, but with less magnitude. The unheated single-phase profile, together with those of low heat flux (i.e., 0–16.0 kW/m^2), showed no significant differences in the velocity profiles. Only small discrepancies for points close to the heater wall were noted. For medium heat fluxes (18.3–35.9 kW/m^2), there was an increase of the axial velocity, extending from $y = 0$ to a distance of about $y = 3.5$ mm. Further increase in the heat flux forced the maximum velocity magnitude to increase and to shift closer to the wall ($y \approx 1$ mm). This behavior was observed for heat fluxes 42.3 and 48.7 kW/m^2. A shift of the maximum velocity location towards the center of the channel started to be observed when reaching a heat flux value of 48.7 kW/m^2. These trends are similar to those of higher heat fluxes cases of the Re = 3309 experiment, except that the "terminal" maximum velocity is now about 0.54 m/s. Fig. 13c shows the profiles of mean liquid axial velocity $\overline{U}$ for Re = 16,549 with wall heat fluxes ranging from 0 to 64 kW/m^2. It is clear that with this Reynolds number, the influence due to heat flux is minimal. The increase of velocity for regions close to the wall as a function of wall heating is less and velocity reduction for regions far from the wall is not noticeable; however, small changes start showing with a wall heat flux of 56.9 kW/m^2, where a noticeable increase of velocity is observed for points in the region from $y = 1.0$ to about 2.5 mm.

7.2. Liquid turbulence statistics

Since most of the changes in the liquid behavior due to wall heating are observed within the boundary layer region, near-wall non-dimensional parameters are utilized. In the wall coordinate system, a characteristic velocity is needed to obtain non-dimensional variables. This characteristic velocity was chosen to be the friction velocity ($u^* = [\tau_w/\rho]^{1/2}$). The friction velocity can be estimated by plotting the dimensional total stress profile and taking a best fit of the near-wall total stress to determine τ_w. Following the previous procedure, single-phase unheated friction velocities were obtained for Re = 3309, 9929, and 16,549. Their values were, respectively, $u^* = 0.012$, 0.027, and 0.040 m/s. All results presented in this section are normalized by the corresponding single-phase unheated friction velocity for each Reynolds number. The measurement uncertainty of the liquid turbulence statistics are presented in the Appendix.

Fig. 14 shows the axial non-dimensional velocity profile ($u^+ = u/u^*$) versus the non-dimensional distance from the wall ($y^+ = yu^*/\nu$) for various values of wall heat fluxes for cases of Re = 3309, 9929, and 16,549. Fig. 14a shows that the unheated single-phase flow case ($q'' = 0$) has a fairly good approximation to the law of the wall.

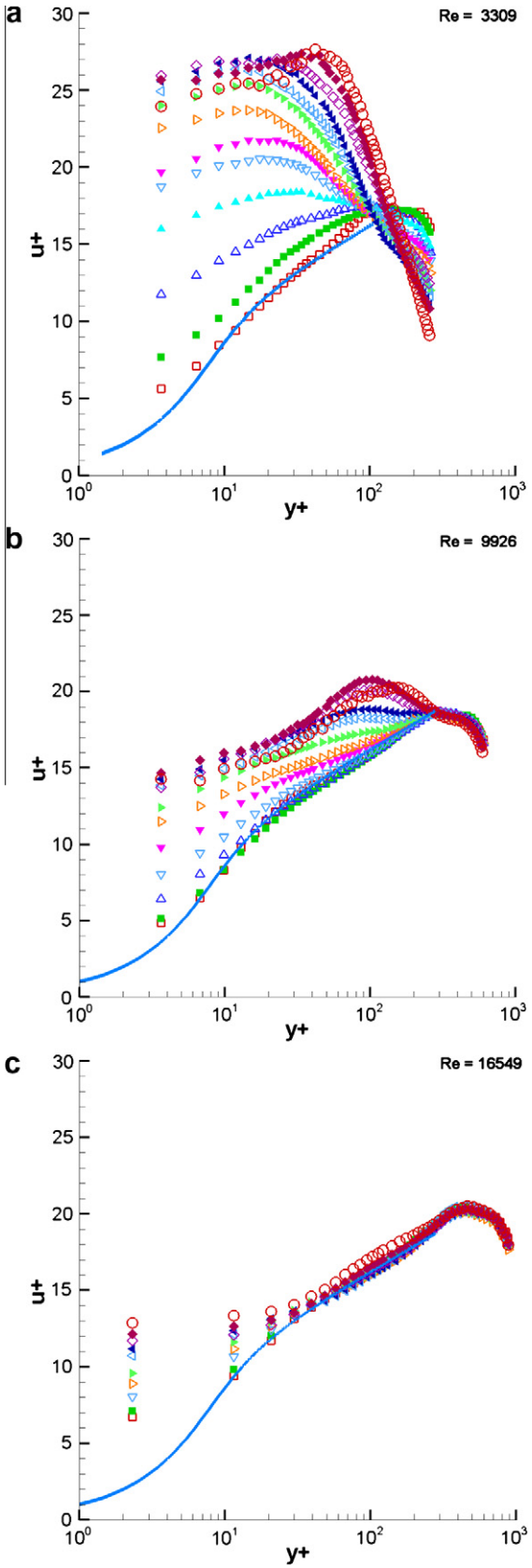

Fig. 14. Mean axial liquid velocity profile normalized with single-phase flow friction velocity for: (a) Re = 3309, $u^* = 0.012$ m/s, (b) Re = 9926, $u^* = 0.027$ m/s, (c) Re = 16,549, $u^* = 0.040$ m/s, with $q'' = 0.0$ □, 3.9 ■, 9.0 △, 12.2 ▲, 16.0 ▽, 18.3 ▼, 20.3 ▷, 22.3 ▶, 35.9 ◁, 42.3 0,0,0.65 ◀, 48.7 0.66,0.0,0.66 ◊, 56.9 ♦, 64.0 ○ (kW/m^2).

Fig. 14b shows that the single-phase profile, together with those of low heat flux (0–9 kW/m^2), showed no significant differences from the law of the wall, and only small discrepancies for points close to the wall heater were observed. For the high Reynolds cases (Fig. 14c), the behavior of the mean velocity was closer to the single-phase flow case, however, for points below $y^+ = 30$ a significant difference is noted. Fig. 15 shows the non-dimensional axial turbulence intensity profile ($u'^+ = u'/u^*$) for various values of wall heating for Re = 3309, 9929, and 16,549. For the low Reynolds number case (Fig. 15a) the heat flux influence is large, including the low heat flux cases. Two trends are observed: first, from $q'' = 3.95$ to 9.02 kW/m^2 there is a decrease in the axial turbulence intensities with respect to the isothermal case, the second trend is observed for the higher heat fluxes where an increase of wall heat flux significantly increase the turbulence intensity. The axial turbulence intensity profiles for the medium Reynolds number (Re = 9929) are presented in Fig. 15b. Two trends were observed here as well, but in this case the first trend persisted for higher heat flux cases, ranging from $q'' = 3.9$ to 22.3 kW/m^2 where the profiles were seen to be below or close to the isothermal case. The starting point for the second trend is shown for wall heat fluxes larger than 35.9 kW/m^2, but a significant increase of the turbulence intensity profile was observed after reaching a wall heat flux of 48.7 kW/m^2. Fig. 15c shows the turbulence intensity profiles for the high Reynolds case (Re = 16,549). Here the wall heat flux influence was dampened and only a small increase of the turbulence intensity profile was observed. No decrease in the axial turbulent intensity was observed below the isothermal case as in the low Reynolds case studied here. Fig. 16 show the non-dimensional normal turbulence intensity profile ($v'+ = v'/u^*$) at various values of wall heat flux for Re = 3309, 9929, and 16,549. These figures showed similar trends as those found for the axial turbulence intensities (u'^+). The two trends discussed previously were observed in Fig. 16a. The first heat flux case $q'' = 3.95$ kW/m^2 showed a decrease on the profile compared to the isothermal case, while the rest of the heat flux cases presented a large increase on turbulence intensity due to the wall heating. Similar behavior was found for the medium and high Reynolds number; however, wall heating influence was reduced while increasing the Reynolds number value. The non-dimensional Reynolds stresses ($u'v'^+ = \overline{u'v'}/u^{*2}$) profiles are shown in Fig. 17 for Re = 3309, 9929, and 16,549. A profile decrease tendency was found as a result of a wall heat flux increment, and a marked shift of the zero location toward the heated wall can be observed. For the low Reynolds number (Fig. 17a) these changes were more pronounced. At the beginning of heating from $q'' = 3.95$–12.23 kW/m^2 a peak reduction and shift of the zero Reynolds stress locations towards the wall was found. Further increase of the heat flux resulted in more reduction in the profile and an inverted peak is observed. The location of this inverted peak (minimum value) will shift towards the center of the channel as a result of the increase of the wall heat flux. The same trends are found for the medium Reynolds number (Fig. 17b), where the profile reduction is more pronounced for points up to $y^+ = 380$. For positions larger than this value, less decrease occurs. The zero shifting and peak inversion is also present. For the highest Reynolds number, the effect of the wall heat flux starts to be noticeable only at high q'' values. There are no significant differences in the profiles up to a heat flux value of 48.7 kW/m^2. For this value of high Reynolds number, the zero value shifting and peak inversion influence were not noted.

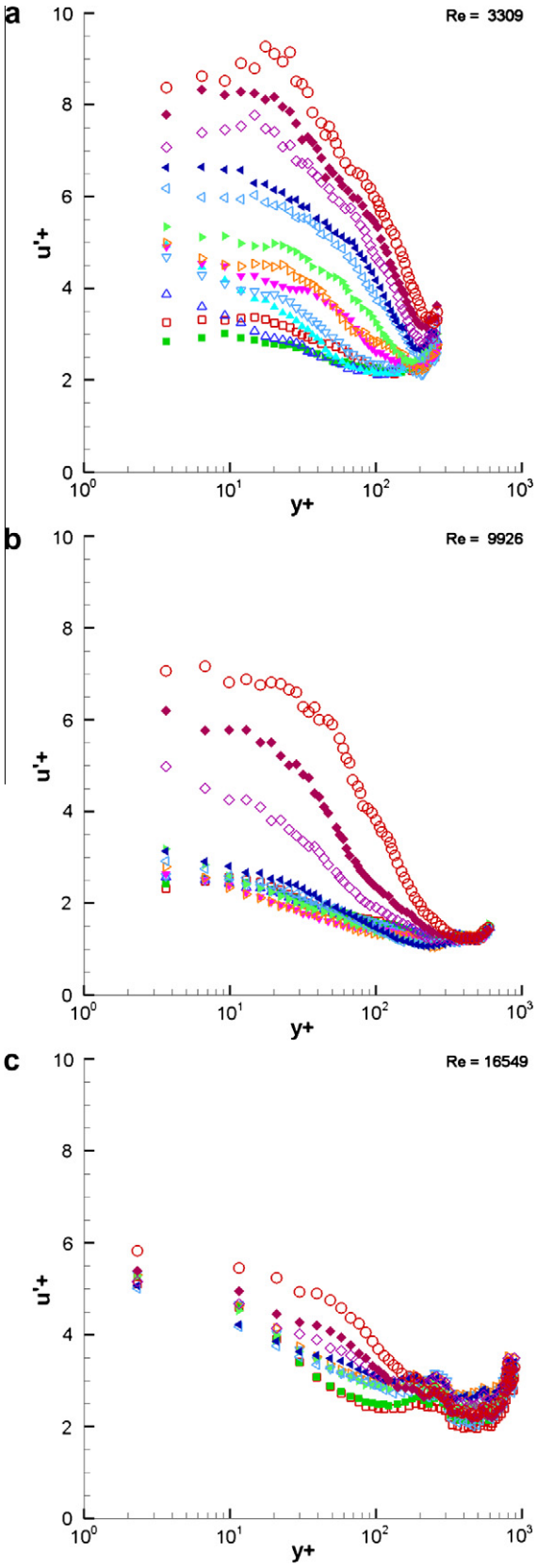

Fig. 15. Mean axial turbulence intensity profile normalized with single-phase flow friction velocity for: (a) Re = 3309, u^* = 0.012 m/s, (b) Re = 9926, u^* = 0.027 m/s, (c) Re = 16,549, u^* = 0.040 m/s, with $q'' = 0.0$ □, 3.9 ■, 9.0 △, 12.2 ▲, 16.0 ▽, 18.3 ▼, 20.3 ▷, 22.3 ▶, 35.9 ◁, 42.3 0,0,0.65 ◀, 48.7 0.66,0.0,0.66 ◊, 56.9 ♦, 64.0 ○ (kW/m^2).

8. Discussion

Some of the mechanisms that govern the fluid behavior are presented and discussed. First, the heated single-phase behavior is ex-

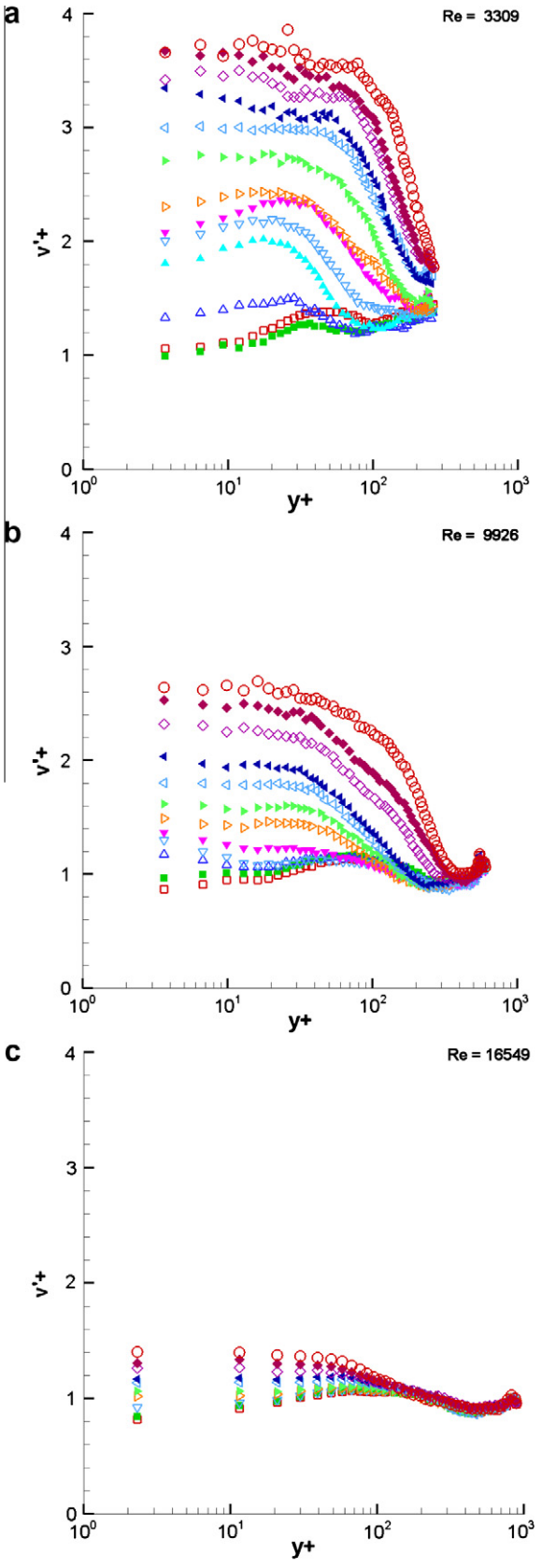

Fig. 16. Mean normal turbulence intensity profile normalized with single-phase flow friction velocity for: (a) Re = 3309, u^* = 0.012 m/s, (b) Re = 9926, u^* = 0.027 m/s, (c) Re = 16,549, u^* = 0.040 m/s, with q'' = 0.0 □, 3.9 ■, 9.0 △, 12.2 ▲, 16.0 ▽, 18.3 ▼, 20.3 ▷, 22.3 ▶, 35.9 ◁, 42.3 0,0,0.65 ◀, 48.7 0.66,0.0,0.66 ◊, 56.9 ♦, 64.0 ○ (kW/m^2).

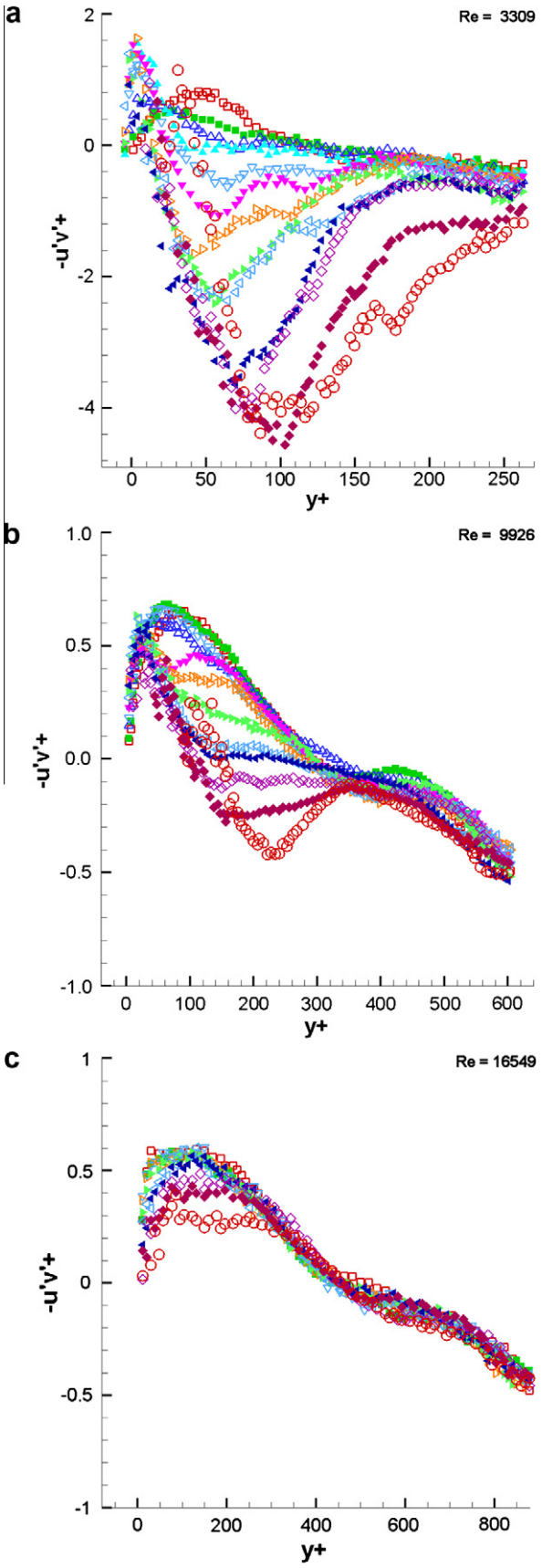

Fig. 17. Reynolds stresses profile normalized with single-phase flow friction velocity for: (a) Re = 3309, u^* = 0.012 m/s, (b) Re = 9926, u^* = 0.027 m/s, (c) Re = 16,549, u^* = 0.040 m/s, with q'' = 0.0 □, 3.9 ■, 9.0 △, 12.2 ▲, 16.0 ▽, 18.3 ▼, 20.3 ▷, 22.3 ▶, 35.9 ◁, 42.3 0,0,0.65 ◀, 48.7 0.66,0.0,0.66 ◊, 56.9 ♦, 64.0 ○ (kW/m^2).

plored to serve as a basis to explain the more complex mechanisms present when subcooled boiling occurs. Previous works have discussed the effects of buoyancy forces on the single-phase heated velocity fields (no boiling involved).

According to Petukhov and Polyakov (1988), the transport of momentum and heat in a boundary layer of a two-dimensional channel flow under the action of gravity is associated with thermogravity effects being manifest via two mechanisms. First, a buoyant force acts over the whole flow as a consequence of the inhomogeneous distribution of mean density. This effect, is called the *external effect*. The second effect includes the direct influence of buoyancy forces on the liquid turbulence due to the fluctuating density in the gravity field. This effect was termed the *structural effect* by Petukhov and Polyakov (1988). They stated that in turbulent mixed convection in a vertical channel, the influence of the structural effect appears first in regions where the viscous forces are surpassed by the buoyancy forces, i.e., outside of the viscous sublayer. This influence can be observed for conditions of low heat flux and high Reynolds number (small Gr/Re^2) such as the low heat flux cases in Fig. 13c; however, a closer look to the experimental data shows a significant influence within the viscous sublayer (see Fig. 14c). The external effect would not be significant during phases of low Gr/Re^2. By increasing the wall heat flux, the external effects are expected to become more pronounced leading to the well-known free convection effect of a higher mean axial velocity profile near the heated wall. For points far from the heated wall, the fluctuating buoyancy force contribution is expected to be negative; the production term, which is positive, decreases in magnitude compared to the isothermal flow. The suppression of turbulence is therefore expected. This effect is shown during the low wall heat flux cases in Fig. 15a) to Fig. 16c. The turbulence intensity suppression was found in all cases except for the higher Reynolds number case (Re = 16,549). For this case a consistent increase with wall heat flux was found.

We now briefly discuss some of the physical implications of the subcooled boiling measurements. Lance and Bataille (1991) suggested that two-phase flow turbulence is the result of interactions between wall turbulence and bubble-induced pseudo-turbulence, the latter being perturbations due to random stirring of the liquid by the bubbles and deformation of their surface. It has been conjectured that these perturbations are proportional to the local vapor fraction and the square of the vapor bubble velocity relative to the liquid. In this study such interactions were found as important modifications to the two-phase flow turbulence statistics profiles, noting new features that were not measured or explained in previous works; for instance, the concomitant increase and shift towards the heated wall of the maximum axial velocity magnitude reached a limit, after which an increase of wall heat flux results in new observed tendencies. Now the maximum axial velocity shifts towards the center of the channel, and its magnitude no longer increases. This behavior is believed to be due to the formation of a fuller bubble layer that will act as a solid wall moving with a speed proportional to the terminal velocity of the near-wall bubbles. Increasing further the heat flux will increase the bubble layer thickness, but not its moving velocity. The bubble layer will result in that both the liquid and its maximum axial velocity position being shifted away from the wall. This behavior was observed on high heat flux and low Reynolds number cases (Fig. 13a).

9. Conclusions

Using PTV, the effect of heat flux on the liquid statistical quantities of subcooled boiling flow was studied. The accuracy of the measurement technique was estimated by various sensitivity studies, proving that PTV is a reliable tool to study subcooled boiling flow. Furthermore, a complete characterization of the flow pattern with various heat fluxes and flow Reynolds numbers was performed; consequently, velocity components, turbulence intensities, and Reynolds stresses under various conditions were obtained as a function of distance from the wall, Reynolds number, and heat flux values. The present results agree with previous works and provides new information due to the full-field nature of the technique. This work is an attempt to provide data of turbulent subcooled boiling flow for validation and improvement of two-phase flow computational models.

Acknowledgments

The authors would like to acknowledge the participation and dedication of Dr. Elvis Dominguez-Ontiveros and Dr. Hee Seok Ahn to make this work possible.

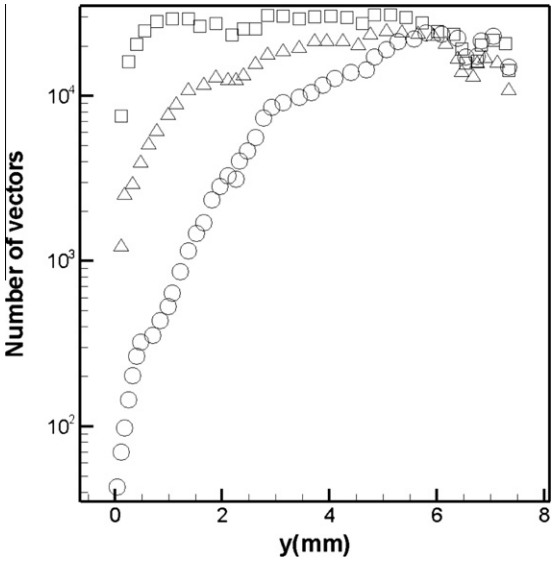

Fig. 18. Number of vectors depending on position from the wall for Re = 3309 with q'' = 0.0 □, 22.3 △, 64.0 ○ kW/m^2.

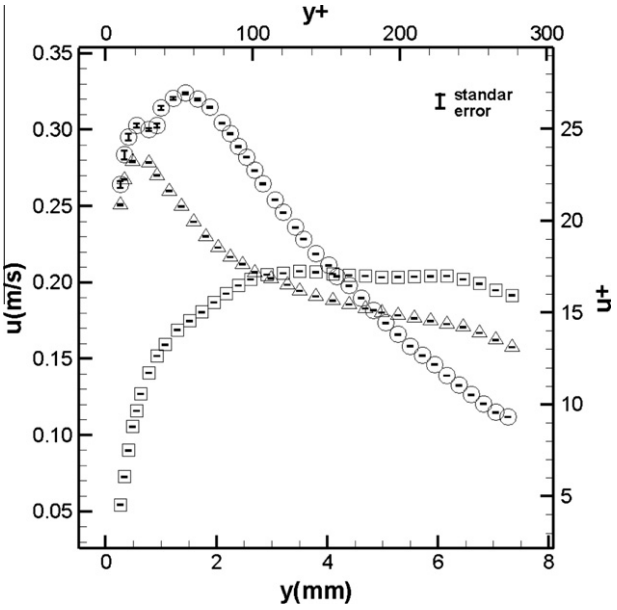

Fig. 19. Mean axial velocity and its standard error for Re = 3309 with q'' = 0.0 □, 22.3 △, 64.0 ○ kW/m^2.

Appendix A. Uncertainty of turbulence statistics

The error analysis presented on the PTV algorithm accuracy section assumed ideal conditions. The effects of large velocity gradients, non-uniform distribution of particles, image noise, wall induced reflections, or any other difficulty that can be encounter in a real PTV experiment, were not considered. To have a better understanding of the uncertainty induced by these effects, three heat flux cases were selected: q'' = 0.0, 22.3, and 64.0 kW/m^2, all with a fixed Reynolds number of Re = 3309. Repeated measurements at these conditions were performed, and uncertainties were estimated from the variance about the sample mean. The measurement uncertainty depends largely on the sample number; in this case, in the number of vectors found at each location. Fig. 18 shows the effect of heat flux on the number of vectors found at different positions from the wall. The number of vectors distribution is mostly uniform for the single-phase flow case (q'' = 0), although in the near-wall region there is a significant decrease of the number of vectors mostly due to wall effects such as wall reflections, high velocity gradients, and loss of correlation of the PTV algorithm. In the boiling flow cases (q'' = 0), the bubble induced reflections and turbulence greatly reduce the number of vectors found. Fig. 19 shows the axial velocity and its accuracy (represented with error bars) for the analyzed cases. The wall and bubble effects showed little influence in the axial velocity accuracy. An uncertainty of less than ±1% was found even for the near-wall region of the high heat flux case. Figs. 20 and 21 show the axial and normal turbulence intensities, respectively, and their uncertainties. Wall and bubble effects have a considerable impact on the uncertainties in the near-wall regions of the high heat flux cases. The maximum uncertainty found was about ±3% for both axial and normal turbulence intensities. Significantly larger uncertainties were found for the Reynolds stresses as shown in Fig. 22. The near-wall region accounted for uncertainties as large as ±20%, therefore points estimated with less than 1000 vectors were discarded.

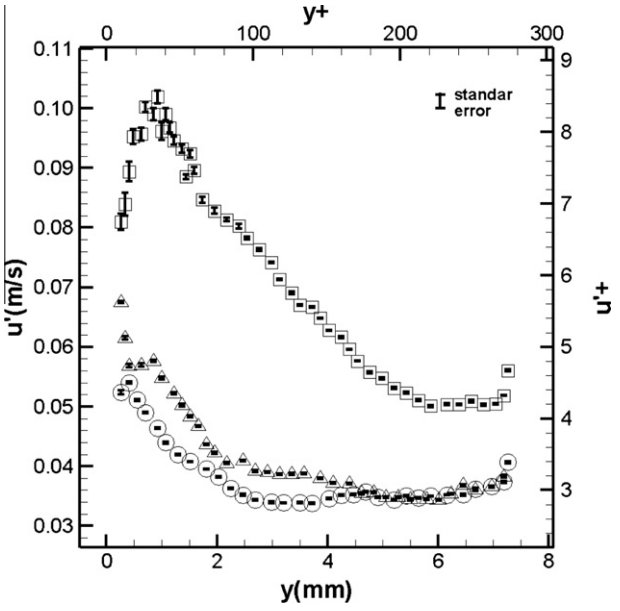

Fig. 20. Mean axial turbulence intensity and its standard error for Re = 3309 with q'' = 0.0 □, 22.3 △, 64.0 ○ kW/m^2.

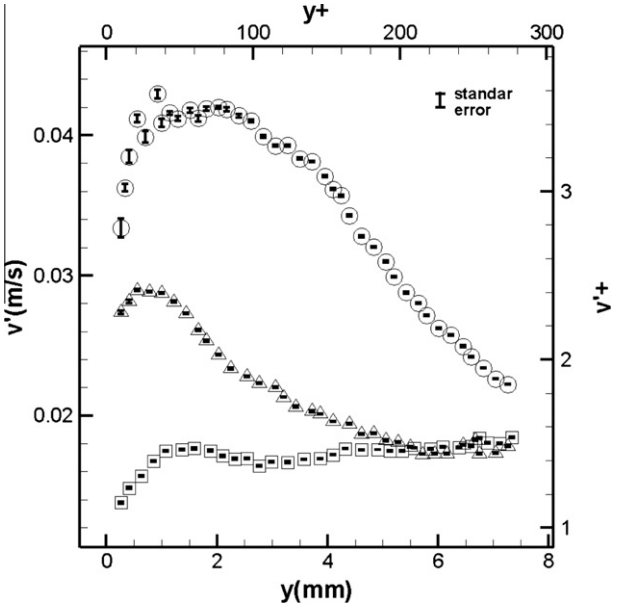

Fig. 21. Mean normal turbulence intensity and its standard error for Re = 3309 with q'' = 0.0 □, 22.3 △, 64.0 ○ kW/m^2.

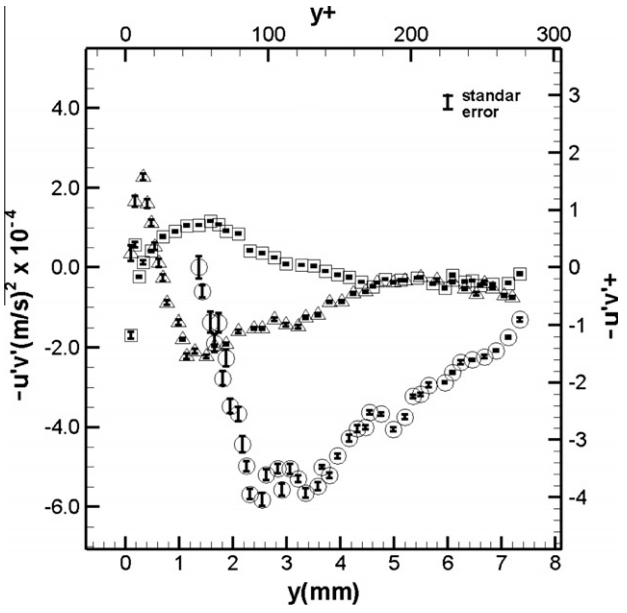

Fig. 22. Reynolds stresses and its standard errors for Re = 3309 with q'' = 0.0 □, 22.3 △, 64.0 ○ kW/m^2.

References

Barrow, H., 1962. An analytical and experimental study of turbulent gas flow between two smooth parallel walls with unequal heat fluxes. Int. J. Heat Mass Transfer 5, 469–487.

Canaan, R., Hassan, Y., 1991. Simultaneous velocity measurements of both components of a two-phase flow using particle image velocimetry. Trans. Am. Nucl. Soc. 63.

Dominguez-Ontiveros, E., Estrada-Perez, C., Ortiz-Villafuerte, J., Hassan, Y., 2006. Development of a wall shear stress integral measurement and analysis system for two-phase flow boundary layers. Rev. Sci. Inst. 77, 105103.

Elsinga, G.E., van Oudheusden, B.W., Scarano, F., 2005. Evaluation of aero-optical distortion effects in PIV. Exp. Fluids 39 (2), 246–256.

Estrada-Perez, C., 2004. Analysis, comparison and modification of various particle image velocimetry (PIV) algorithms. Master thesis, Texas A&M University, TX, USA.

Gui, L., Wereley, S.T., 2002. A correlation-based continuous window shift technique to reduce the peak-locking effect in digital PIV image evaluation. Exp. Fluids 32, 506–517.

Hasan, A., Roy, R., Kalra, S., 1992. Velocity and temperature fields in turbulent liquid flow through a vertical concentric annular channel. Int. J. Heat Mass Transfer 35 (6), 1455–1467.

Hassan, Y., Gutierrez-Torres, C., Jimenez-Bernal, J., 2005. Temporal correlation modification by microbubbles injection in a channel flow. Int. Commun. Heat Mass Transfer 32 (8), 1009–1015.

HFE-301 3M, 2009. Product information, 3M Novec 7000, engineered fluid. <http://multimedia.mmm.com/mws/>.

Kang, S., Patil, B., Zarate, J., Roy, R., 2001. Isothermal and heated turbulent upflow in a vertical annular channel – part i. Experimental measurements. Int. J. Heat Mass Transfer 44 (6), 1171–1184.

Kline, S., McClintock, F., 1953. Describing uncertainties in single-sample experiments. Mech. Eng. 75 (1), 3–8.

Končar, B., Kljenak, I., Mavko, B., 2004. Modelling of local two-phase flow parameters in upward subcooled flow boiling at low pressure. Int. J. Heat Mass Transfer 47 (6–7), 1499–1513.

Koyasu, M., Tanaka, T., Sato, Y., Hishida, K., 2009. Turbulence structure of bubbly upward flow (high spatial and temporal resolution measurements using high speed time series PTV). Trans. Jpn. Soc. Mech. Eng., Part B 75 (755), 1446–1453 (in Japanese).

Lance, M., Bataille, J., 1991. Turbulence in the liquid phase of a uniform bubbly air–water flow. J. Fluid Mech. 222, 95–118.

Lee, T., Park, G., Lee, D., 2002. Local flow characteristics of subcooled boiling flow of water in a vertical concentric annulus. Int. J. Heat Mass Transfer 28 (8), 1351–1368.

Mayinger, F., 1981. Scaling and modeling laws in two-phase flow and boiling heat transfer. Two-Phase Flow and Heat Transfer in the Power and Process Industries, vol. 1. Hemisphere Publishing Corporation, Washington, DC. pp. 424–454 (Chapter 14).

Noback, H., Honkanen, M., 2005. Two-dimensional Gaussian regression for sub-pixel displacement estimation in particle image velocimetry or particle position estimation in particle tracking velocimetry. Exp. Fluids 38 (4), 511–515.

Ortiz-Villafuerte, J., Hassan, Y., 2006. Investigation of microbubble boundary layer using particle tracking velocimetry. J. Fluid Mech. 128, 507.

Petukhov, B., Polyakov, A., 1988. Heat Transfer in Turbulent Mixed Convection. Hemisphere, Washington.

Ramstorfer, F., Steiner, H., Brenn, G., 2008. Modeling of the microconvective contribution to wall heat transfer in subcooled boiling flow. Int. J. Heat Mass Transfer 51, 4069–4082.

Riethmuller, M., 2000. Particle Image Velocimetry and Associated Techniques. von Karman Institute for Fluid Dynamics Rhode St. Genese, Belgium.

Roy, R., Hasan, A., Kalra, S., 1993. Temperature and velocity fields in turbulent liquid flow adjacent to a bubbly boiling layer. Int. J. Multiphase Flow 19 (5), 765–795.

Roy, R., Kang, S., Zarate, J., Laporta, A., 2002. Turbulent subcooled boiling flow experiments and simulations. J. Heat Transfer 124, 73.

Roy, R., Krishnan, V., Raman, A., 1986. Measurements in turbulent liquid flow through a vertical concentric annular channel. J. Heat Transfer 108, 216–218.

Roy, R., Velidandla, V., Kalra, S., 1997. Velocity field in turbulent subcooled boiling flow. J. Heat Transfer 119, 754.

Scarano, F., Riethmuller, M., 2000. Advances in iterative multigrid PIV image processing. Exp. Fluids 29, 51–60.

Serizawa, A., Kataoka, I., Michiyoshi, I., 1975a. Turbulence structure of air–water bubbly flow – I. Measuring techniques. Int. J. Multiphase Flow 2 (3), 221–233.

Serizawa, A., Kataoka, I., Michiyoshi, I., 1975b. Turbulence structure of air–water bubbly flow – II. Local properties. Int. J. Multiphase Flow 2 (3), 235–246.

Serizawa, A., Kataoka, I., Michiyoshi, I., 1975c. Turbulence structure of air–water bubbly flow – III. Transport properties. Int. J. Multiphase Flow 2 (3), 247–259.

Situ, R., Hibiki, T., Sun, X., Mi, Y., Ishii, M., 2004. Flow structure of subcooled boiling flow in an internally heated annulus. Int. J. Heat Mass Transfer 47 (24), 5351–5364.

Stanislas, M., Okamoto, K., Kähler, C., Westerweel, J., Scarano, F., 2008. Main results of the third international PIV challenge. Exp. Fluids 45 (1), 27–71.

Takehara, K., 1998. A study on particle identification in PTV particle mask correlation method. J. Visual. 1 (3), 313–323.

Velidandla, V., Putta, S., Roy, R., 1996. Turbulent velocity field in isothermal and heated liquid flow through a vertical annular channel. Int. J. Heat Mass Transfer 39, 3333–3346.

Wardana, I., Ueda, T., Mizomoto, M., 1992. Structure of turbulent two-dimensional channel flow with strongly heated wall. Exp. Fluids 13 (1), 17–25.

Wardana, I., Ueda, T., Mizomoto, M., 1994. Effect of strong wall heating on turbulence statistics of a channel flow. Exp. Fluids 18 (1), 87–94.

Willert, C., Gharib, M., 1991. Digital particle image velocimetry. Exp. Fluids 10 (4), 181–193.

Yeoh, G., Tu, J., Lee, T., Park, G., 2002. Prediction and measurement of local two-phase flow parameters in a boiling flow channel. Numer. Heat Transfer, Part A 42 (1), 173–192.

Zarate, J., Capizzani, M., Roy, R., 1998. Velocity and temperature wall laws in a vertical concentric annular channel. Int. J. Heat Mass Transfer 41, 287–292.